Development of a three-dimensional variational assimilation system for lidar profile data based on a size-resolved aerosol model in WRF-Chem model v3.9.1 and its application in $PM_{2.5}$ forecasts across China

Yanfei Liang[1,2], Zengliang Zang[1], Dong Liu[3], PengYan[4], Yiwen Hu[5], Yan Zhou[6], Wei You[1]

[1]Institute of Meteorology and Oceanography, National University of Defense Technology, Nanjing, China.
[2]No.32145 Unit of PLA, Xinxiang, China
[3]Key Laboratory of Atmospheric Optics, Anhui Institute of Optics and Fine Mechanics, Chinese Academy of Sciences, Hefei, China
[4]Meteorological Observation Center, Chinese Meteorological Administration, Beijing, China
[5]Nanjing University of Information Science & Technology, Nanjing, China
[6]No.78127 Unit of PLA, Beijing, China

*Corresponding author: Wei You (ywlx_1987@163.com); Zengliang Zang (zzlqxxy@163.com)

Abstract:

The authors developed a three-dimensional variational (3-DVAR) aerosol extinction coefficient (AEC) and aerosol mass concentration (AMC) data assimilation (DA) system for aerosol variables in the Weather Research and Forecasting–Chemistry (WRF–Chem) model with the WRF–Chem using the Model for Simulating Aerosol Interactions and Chemistry (MOSAIC) scheme. They establish an AEC observation operator and its corresponding adjoint based on the Interagency Monitoring of Protected Visual Environments (IMPROVE) equation and investigate the use of lidar AEC and surface AMC DA to forecast mass concentration (MC) profiles of $PM_{2.5}$ (particulate matter with an aerodynamic diameter of less than 2.5 μm) across China. Two sets of data were assimilated: AEC profiles captured by five conventional Mie scattering lidars (positioned in Beijing, Shijiazhuang, Taiyuan, Xuzhou, and Wuhu) and $PM_{2.5}$ and PM_{10} MC data obtained from over 1,500 ground environmental monitoring stations across China. Three DA experiments (i.e., a $PM_{2.5}$(PM_{10}) DA experiment, a lidar AEC DA experiment, and a simultaneous $PM_{2.5}$(PM_{10}) and lidar AEC DA experiment) with a 12 h assimilation period and a 24 h forecast period were conducted. The $PM_{2.5}$(PM_{10}) DA reduced the root mean square error (RMSE) of the surface $PM_{2.5}$MC in the initial field of the model by 38.6μg/m^3 (64.8%). When lidar AEC data were assimilated, this reduction was 10.5μg/m^3 (17.6%), and a 38.4μg/m^3 (64.4%) reduction occurred when the two data sets were assimilated simultaneously, although only five lidars were available within the simulation region (approximately 2.33 million km^2 in size).The RMSEs of the forecasted surface $PM_{2.5}$MC 24 h after the DA period in the three DA experiments were reduced by 6.1μg/m^3 (11.8%), 1.5μg/m^3 (2.9%), and 6.5μg/m^3 (12.6%), respectively, indicating that the assimilation and hence the optimization of the initial field have a positive effect on the $PM_{2.5}$MC forecast performance over a period of 24 h after the DA

period.

1. Introduction

Aerosol data assimilation (DA) generates a three-dimensional (3D) gridded analysis field capable of describing the spatial distribution of aerosols by integrating numerical forecasts produced by an air quality model (AQM) and measured aerosol data. With integrated information from various sources, this analysis field can more accurately describe the 3D distribution pattern of aerosols (Carmichael et al., 2008; Benedetti et al., 2009; Sandu et al., 2011; Bannister, 2017). The analysis field generated by DA can be used to effectively study atmospheric aerosol transmission patterns through an analysis of the products of a certain time series and, on this basis, further examine the effects of aerosols on human health, the environment, the weather, and the climate (Baraskar et al., 2016). The analysis field can also be used to determine the initial chemical conditions for an AQM. Therefore, improving the accuracy of the initial chemical conditions and enhancing the forecasting performance of the AQM for aerosols (Wu et al., 2015).

Compared to those of meteorological and marine DA, aerosol DA techniques are still undeveloped, and there is a lack of variety when it comes to assimilable measured data, which mainly include conventional surface aerosol mass concentration (AMC) data and satellite-derived aerosol optical depth (AOD) data. Of these two types of data, surface AMC data provide mass concentration (MC) information for near-surface aerosols directly. AOD is a measure of the total extinction effects of aerosols in the vertical atmospheric column, which indirectly provide atmospheric column aerosol concentration information. Assimilating either of these two types of data can significantly improve the accuracy of the aerosol analysis field (Tombette et al., 2008; Niu et al., 2008; Schwartz et al., 2012; Jiang et al., 2013; Li et al., 2013; Saide et

al., 2013; Yumimoto et al., 2015, 2016; Tang et al., 2017; Peng et al., 2016; Xia et al.,2019; Wang et al., 2020). However, neither AOD nor surface AMC data are able to provide vertical aerosol profiles. Consequently, while these two types of data are abundant, have relatively high horizontal resolutions, and have excellent coverage, they play a limited role in optimizing the vertical structure of aerosols in the analysis field. To further improve the accuracy of the simulated vertical structure, it is necessary to assimilate data that contain vertical aerosol profile information. Zang et al. (2016) assimilated aircraft-measured vertical concentration profiles of aerosol components and found that while the profile data were limited in quantity and covered a relatively small area, they could still significantly improve the forecast accuracy of an AQM. Since direct observations of concentration profiles are labor-intensive and expensive, relatively few studies involving the acquisition and assimilation of this type of data have been reported.

Aerosol lidar can be used to capture aerosol-backscattered laser signals at various heights. By inverting these signals, the aerosol extinction coefficient (AEC) and aerosol backscattering coefficient (ABC), which indirectly provide vertical AMC profile information, can be determined (Fernald et al., 1984; Sugimoto et al., 2008, Raut et al., 2009). Assimilating these lidar aerosol data can help to improve the accuracy of the vertical structure of aerosols in the analysis field (Tesche et al., 2007; Dilip et al., 2009; Young, S. A., and M. A. Vaughan, 2009; Burton et al., 2010; Milroy et al., 2011; Sugimoto et al., 2014; Chen et al., 2015). In addition, with the increasing number of lidar stations and the development of lidar network detection technology, studying lidar DA in order to generate more accurate 3D aerosol analysis fields has great potential.

Compared to the assimilation of direct AMC measurements, the assimilation of lidar AEC data faces myriad difficulties, of which establishing an observation operator for the DA cost function is the most challenging. The

AEC is the object of the DA (i.e., observation variable), whereas the AMCs of various types of aerosol variables in the AQM must be optimized. To directly determine the optimal model aerosol variables by solving the DA cost function, it is necessary to map the aerosol variables in the AQM to the observation space by conducting a forward process on the observation operator (Kahnert et al., 2008), corresponding to the calculation of the AEC from the AMC. In addition, in 3-DVAR DA, it is also necessary to conduct the adjoint process on the observation operator when calculating the gradient of the cost function (Sandu et al., 2011). The computational program for this adjoint process on the observation operator relies on its forward process, leading to a large computational load, and the size of the program code increases nonlinearly with the complexity of the forward process. Moreover, when it comes to aerosol variables, there are many kinds of chemicals and particle-size bins so that the chemical model inherently involves a large computational load. Therefore, when using a variational method to assimilate lidar data, it is necessary to consider both the accuracy and complexity of the observation operator. Currently, there are three main methods that are used to design observation operators: (1) use of the Mie equation directly. Under the assumption that aerosol particles are uniform and spherical, the Mie equation describes the scattering and extinction properties of aerosol particles of any scale with any chemical and physical parameters (Cheng et al., 2019). However, because accurately solving the Mie equation involves a nonlinear calculation process that contains iterations, it is extremely complicated to implement, upgrade, and maintain the program for the reverse process on the observation operator. In addition, because of the lack of reliable measurements of essential aerosol parameters (e.g., complex refractive index, particle number spectrum, and hygroscopicity), it is necessary to introduce assumptions about these parameters in DA schemes. This renders it difficult to realize the high-accuracy advantage of DA schemes in practice; (2) use of the

Community Radiative Transfer Model (CRTM). This model is advantageous because it gives the Jacobian term needed for the adjoint process on the observation operator when conducting its forward process. Therefore, introducing the CRTM to a DA scheme does not require separate numerical computational programming for the adjoint process on the observation operator (Liu and Weng, 2006). DA schemes based on the CRTM have been applied in AOD DA research and yielded excellent results (Liu et al., 2011). However, the CRTM was developed for the Goddard Chemistry Aerosol Radiation and Transport (GOCART) aerosol scheme in the Weather Research and Forecasting–Chemistry (WRF–Chem) model. As a result, when applying the CRTM to other AQMs and aerosol schemes, it is necessary to design corresponding variable transformation interfaces (Cheng et al., 2019), which introduces additional errors; (3) use of the interagency monitoring of protected visual environments (IMPROVE) equation. The IMPROVE equation maps the relationship between the AMC and the AEC (Lowenthal et al., 2003; Ryan et al., 2005; Pitchford et al., 2007; Gordon et al., 2018).With relatively high computational accuracy, this method has been used to evaluate model performance and the extinction contributions of various aerosols (Kim et al., 2006; Roy et al., 2007; Tao et al., 2009, 2012, 2014; Cao et al., 2012a, 2012b). In addition, as its highest-order term is quadratic, the IMPROVE equation has low nonlinearity. Therefore, using the IMPROVE equation to design an observation operator can significantly reduce the complexity of the DA program. To date, no observation operator design based on the IMPROVE equation and subsequent variational lidar DA have been reported.

Some progress has been made in lidar DA. For example, Sekiyama et al. (2010) used the Kalman filter DA method to assimilate the ABC and AEC profiles acquired by the Cloud-Aerosol Lidar and Infrared Pathfinder Satellite Observations mission and applied the assimilated data to a global chemical

transport model. Wang et al. (2013, 2014a, and 2014b) studied the assimilation of range-corrected lidar signals using the optimal interpolation DA method and conducted an assimilation experiment based on data captured by 12 lidars positioned in the Mediterranean Basin from the ACTRIS (Aerosols, Clouds, and Trace Gases Research InfraStructure)/EARLINET (European Aerosol Research Lidar Network) and one lidar positioned on the French Corsicain from the framework of the pre-ChArMEx (Chemistry-Aerosol Mediterranean Experiment)/TRAQA (TRAnsport àlongue distance et Qualité de l'Air). They found that DA improved the $PM_{2.5}$ forecast performance for approximately 36 hours. However, in the above-mentioned studies, sequential DA methods were used, and there was no particular need to take into consideration the complexity of the observation operator. Cheng et al. (2019) assimilated lidar AEC profiles using a 3-DVAR DA method with an observation operator based on the CRTM that was designed for a relatively simple GOCART dust aerosol scheme.

This study presents an observation operator and corresponding adjoint module developed for lidar AEC DA based on the IMPROVE equation, which was introduced into the DA system by Li et al. (2013) and Zang et al. (2016) for the Model for Simulating Aerosol Interactions and Chemistry (MOSAIC) aerosol scheme oriented to the WRF–Chem model. By applying the DA system, DA and forecast experiments were conducted to investigate the application of lidar AEC DA in $PM_{2.5}$ forecasts across China based on data captured by five lidars (located in Beijing, Shijiazhuang, Taiyuan, Xuzhou, and Wuhu, respectively) as well as on $PM_{2.5}$ and PM_{10} data collected at approximately 1,500 ground environmental monitoring stations across China.

2. Materials and Methods

2.1. AQM

The WRF–Chem model version 3.9.1 was selected as the AQM. The model has 40 vertical layers between the surface and 50 hPa, with the resolution gradually decreasing from the bottom up. The model domains are double-nested, and the second domain (D02) is centered at (114.57°E, 37.98°N) and has 175×166 grid points with a grid interval of 9 km. D02 covers the central and eastern regions of China (most of North China, northern Central China, northern East China, and eastern Northwest China) (Figure 1). The MOSAIC_4bin aerosol scheme was adopted for the simulations. This scheme, which will be described in Section 2.4, can be used to predict the profiles of eight aerosol types. For each aerosol type, there are four particle-size bins (4bins). The following summarizes the other physical and chemical schemes used in this study: the carbon-bond mechanism version Z (CBMZ) chemical reaction mechanism, the fast-J photolysis calculation scheme, the rapid radiative transfer model for general circulation models (RRTMG) shortwave radiation scheme, the RRTMG longwave radiation scheme, the WRF single-moment5-class microphysical scheme, the unified Noah land-surface parameterization scheme, the Grell 3D ensemble cumulus parameterization scheme, the Yonsei University planetary boundary layer scheme, and the revised MM5 Monin-Obukhov near-surface layer scheme.

2.2. Data

The AEC profiles used in this study were derived from data captured by five conventional Mie scattering lidars (positioned in Beijing, Shijiazhuang, Taiyuan, Xuzhou, and Wuhu, Figure 1) at a wavelength of 532 nm between 0000 and 1200 Coordinated Universal Time (UTC) on November 13, 2018 (Chen et al., 2019; Zhang et al., 2020). The temporal resolution of the data measured by the lidars in Shijiazhuang, Taiyuan, Xuzhou, and Wuhu was 1 min, that is, data were captured, and a vertical AEC profile was derived every minute. The vertical resolution of these data was 7.5 m, that is, one AEC was

determined in one profile 7.5m away from the next one. The blind zone of these lidars was 100 m, that is, these systems could not effectively capture AEC data between the surface and the height of 100 m. The temporal and vertical resolutions of the AEC profiles captured by the lidar in Beijing were 1 h and 15 m, respectively, and the blind zone of this lidar was 210 m. The relative standard deviation of the aerosol parameter profiles captured by the lidar over Beijing was 20.4% in the height range of 1-2 km. This lidar was calibrated via comparative observation of several lidars (Chen et al., 2019). The precision of the AEC profiles released by the other four lidars was below the quality margins (25% of the typical AEC observed in the planetary boundary layer or $\pm 0.01 km^{-1}$), as defined by Matthias et al. (2004). However, the relative standard deviation of the aerosol parameter profiles in the height range of 2-5 km released by lidar over Beijing was 35.9%. To improve the effectiveness of the DA, it was necessary to first perform quality control on and preprocess the original AEC profiles. This ensured that the lidar data matched the numerical model in terms of temporal and spatial resolution. Quality control involved four steps: (1) Entire AEC profiles passing through low clouds and AEC measurements in mid- and high-cloud regions were eliminated. Clouds were defined as regions in which the AEC was higher than $5{,}000\times10^{-6}$ m^{-1}(assuming the AEC in the near-surface layer (below 150 m) was lower than $3{,}000\times10^{-6}$ m^{-1}); (2) AEC profile data were subjected to maximum and minimum control. AEC measurements higher than $3{,}000\times10^{-6}$ m^{-1} were each reassigned with a value of $3{,}000\times10^{-6}$ m^{-1}. AEC measurements lower than 20×10^{-6} m^{-1} were eliminated; (3) For spatial continuity, data was required to be continuous within a vertical space L_{con}, which was set to be 90 m in this study. Specifically, two metrics were used to examine the spatial continuity of the data. First, the profile with vertical resolution L_{res} was examined. After the first two steps of quality control, the remaining number of data points (N_{remain}) within the L_{con} could not be less than one-third the total

number of data points within the L_{con} (N_{total}= L_{con}/L_{res}). Otherwise, no valid data would be available for the center of the L_{con}. Second, the deviation of the valid data from the mean value of the data within the L_{con} could not exceed three times the standard deviation (SD); (4) Data within the blind zone of a lidar were eliminated. In addition, because lidar signals are relatively weak and AMCs are extremely low above 5,000 m, data for the region above 5,000 m were also eliminated in this study. After the quality control process, 84.32% of the original AEC data from the lidar over Beijing were accepted as valid data, and 88.75%, 54.10%, 26.74%, and 10.95% of the data from the Taiyuan, Wuhu, Shijiazhuang, and Xuzhou lidars, respectively, were valid.

Preprocessing of quality control-treated AEC profiles involved two steps: (1) Temporal and spatial smoothing. Profiles were subjected to moving averaging over 30 m in the vertical direction. Temporally, the AEC profiles were averaged over the previous hour; (2) Data thinning. If there were multiple data points between two adjacent model layers in the vertical direction, only one was selected for assimilation. In this study, the nearest data point below each model layer was selected for assimilation. After processing, the number of assimilated AEC measurements per profile did not exceed 25, as there were no more than 25 model layers between the top of the lidar blind zone and the height of 5,000 m.

$PM_{2.5}$ and PM_{10} data (hereinafter referred to as PM data) used in this study, including 1-h MC data collected at more than 1,500 ground environmental monitoring stations, originated from the China National Environmental Monitoring Center. Most of the monitoring stations were distributed in cities in economically developed regions, including the Yangtze River Delta, the Beijing–Tianjin–Hebei region, and the Pearl River Delta. Of these monitoring stations, more than 790 were located within the D02 region (Figure 1). The assimilated PM data were collected between 0000 and 1200

UTC on November 13, 2018. After assimilation, forecasts for $PM_{2.5}$ from 1200 UTC on November 13, 2018 to 1200 UTC on November 14, 2018 were produced. In addition, the effects of DA on the forecast performance of the model were evaluated based on surface $PM_{2.5}$ measurements. To improve the DA performance and the representativeness of the evaluation metrics, the original PM data were subjected to quality-control and preprocessing treatments. Quality control involved two main steps: (1) Anomalous elimination. Measurements that remained unchanged over a continuous period of 24 h were considered anomalous and removed. (2) Maximum and minimum control. $PM_{2.5}$MC measurements higher than 600 μg/m^3, PM_{10}MC measurements higher than 1,200 μg/m^3, and PM MC measurements less than 0 were considered anomalies and were removed. During the DA and verification processes, there could be multiple PM MC measurements for one grid cell. To allow the measurements to represent the average PM MC within a certain area, the PM data used for DA and verification were subjected to grid-cell averaging. The PM data used for assimilation were averaged within 5×5 grid cells. Specifically, the PM data within the same 5×5 grid cell area were first examined to determine their spatial consistency. Data greater than twice the SD were removed. Next, the arithmetic mean of the data within the area was calculated and assimilated. The $PM_{2.5}$MC measurements used for verification and model forecasts were averaged within 1×1 grid cells. Specifically, model forecasts were first interpolated to the location of each ground environmental monitoring station. Next, the arithmetic mean of the measured and forecasted values within the same grid cell was calculated and used as a sample for quantifying the evaluation metrics. The processed PM MC data for the D01 and D02 regions were assimilated, while only the $PM_{2.5}$MC data for the D02 region were used to evaluate the effects of the DA. After the grid-cell averaging treatment, approximately 190 data points in the D02 region were assimilated each time.

2.3. Basic theoretical DA model

To mathematically achieve 3-DVAR DA, it is necessary to establish an objective function to transform the DA problem to a problem of finding the extreme values of the function. By calculating the extreme values of the function using the variational method, an "optimal" analysis field is obtained. The following shows the mathematical form of such a function:

$$\mathrm{J}(x)=\frac{1}{2}(x-x^b)^T B^{-1}(x-x^b)+\frac{1}{2}(Hx-y)^T R^{-1}(Hx-y) \quad (1)$$

This function describes the sum of the distance between the analysis field (x) and the background field (x^b) and the distance between the analysis field (x) and the observation field (y), with the background error covariance B and the observation error covariance R as weights, respectively. In Equation (1), x is the control variable in the DA system, which is a one-dimensional (1D) vector composed of aerosol variables at all the 3D grid cells in the DA analysis field; x^b is the background value (or best guess) of the control variable (as the forecast level of AQM increases, model forecasts are generally used as background fields); B is the background error covariance; y is the observation variable, which is a 1D vector composed of all the measurements; H is the observation operator, which maps the control variable to the observation space to ensure that the observation data can provide observation information for the control variable even if they are not direct measurements of the control variable; and R is the observation error covariance. For simultaneous assimilation of two or more types of observation data, the second term on the right side of Equation (1) can be expanded to multiple terms, each of which corresponds to one type of observation data. This will facilitate the simultaneous assimilation of observational data from various sources.

2.4. Control variables and B

The MOSAIC_4bins aerosol scheme adopted in this study accommodated eight aerosol types, namely, black/elemental carbon (EC/BC), organic carbon (OC), sulfates ($SO4^{2-}$), nitrates($NO3^{-}$), ammonium salts($NH4^{+}$), chlorides(Cl^{-}), sodium salts(Na^{+}), and other unclassified inorganic compounds (OIN). There were four particle-size bins (4bin) for each aerosol type, namely, 0.039–0.1, 0.1–1.0, 1.0–2.5, and 2.5–10 μm. Thus, there were 32 model variables that represented the various aerosols. However, limitations in computer memory and computational capacity necessitated a reduction in the total number of control variables. In addition, the AECs of fine ($PM_{2.5}$) and coarse ($PM_{2.5–10}$) particles differed significantly. Thus, two control variables for each aerosol type were designed—one corresponding to fine particles (formed by combining the first three particle-size bins) and one corresponding to coarse particles (the fourth particle-size bin). Thus, there were 16 control variables in the DA scheme, namely, $EC_{2.5}$, $EC_{2.5\text{-}10}$, $OC_{2.5}$, $OC_{2.5\text{-}10}$, $SO4_{2.5}$, $SO4_{2.5\text{-}10}$, $NO3_{2.5}$, $NO3_{2.5\text{-}10}$, $NH4_{2.5}$, $NH4_{2.5\text{-}10}$, $CL_{2.5}$, $CL_{2.5\text{-}10}$, $NA_{2.5}$, $NA_{2.5\text{-}10}$, $OIN_{2.5}$, and $OIN_{2.5\text{-}10}$.

There were two problems associated with calculations involving *B*: (1) In this scheme, *B* contained 3.5×10^{14} ((square of 16 (number of control variables) ×175×166×40 (number of grid cells)) elements. Thus, it was necessary to mathematically treat and simplify *B* to facilitate numerical calculations. Following the method used by Li et al. (2013) and Zang et al. (2016), *B* was decomposed into a background-error standard deviation (BESD) matrix, a background-error horizontal correlation coefficient (BEHCC) matrix, and a background-error vertical correlation coefficient (BEVCC) matrix for calculations; (2) As the true value of *B* was unknown, it was necessary to develop a reasonable statistical method to estimate it. The National Meteorology Center (NMC) method (Parrish and Derber, 1992) was employed in this study to statistically estimate *B*. Specifically, the differences between

the 48h and 24h forecasts of the control variables were assumed to be a proxy of the background error. Next, *B* was estimated based on the covariance of the difference field, which was obtained by producing continuous 24 h and 48 h forecasts for a month using the WRF–Chem model.

2.5. Observation operator and its ajoint

Obtaining the observation operator involved two calculations: (1) The control variables at each grid cell were mapped to the observation space, that is, the control variables were mapped to the AEC values (or $PM_{2.5}$ and PM_{10}MCs); (2) The mapped values at the eight vertices of the model grid cell associated with the observation data were interpolated using the inverse distance-weighted method to the observation location. Here, we only describe the first step of the derivation of the observation operators, which are different for different observation data.

The AEC observation operator was based on the IMPROVE equation. The following shows the specific form of the IMPROVE equation:

$$\begin{aligned} Ext = {} & 3.025 \times fs(RH) \times [Small\ Sulfate] + \\ & 6.6 \times fl(RH) \times [Large\ Sulfate] + \\ & 3.096 \times fs(RH) \times [Small\ Nitrate] + \\ & 6.579 \times fl(RH) \times [Large\ Nitrate] + \\ & 5.04 \times [Small\ Organic\ Mass] + \\ & 10.98 \times [Large\ Organic\ Mass] + \\ & 10.0 \times [Elemental\ Carbon] + \\ & 1.0 \times [Fine\ Soil] + \end{aligned} \tag{2}$$

$$1.7 \times fss(RH) \times [Sea\ Salt] +$$

$$1.0 \times [Coarse\ Mass]$$

The left side of Equation (2) is the AEC value *Ext* (unit: 10^{-6} m^{-1}). The variables in the brackets on the right side of Equation (2) are combinations of the 16 control variables (unit: μg/m^3). The coefficient variables *fs*(*RH*), *fl*(*RH*), and *fss*(*RH*) reflect the effects of hygroscopicity of fine, coarse, and sea-salt aerosols, respectively, under various relative humidity (HR) conditions. The values of the parameters given by Gordon et al. (2018) were used in this study. The variables (in square brackets) at each grid cell were obtained by combining the 16 control variables using the following method:

$$Sulfate = SO4_{2.5} + \alpha \times NH4_{2.5}.$$

The principle for determining α involved preferentially allocating $NH4_{2.5}$ to $SO4_{2.5}$. The remaining $NH4_{2.5}$ was allocated to $NO3_{2.5}$.

$$[Small\ \ Sulfate] = \begin{cases} 0 & , Sulfate >= 20 \\ (1 - \frac{Sulfate}{20}) \times Sulfate & , Sulfate < 20 \end{cases}$$

$$[Large\ Sulfate] = Sulfate - [Small\ Sulfate]$$

$$Nitrate = NO3_{2.5} + (1-\alpha) \times (NH4_{2.5})$$

$$[Small\ \ Nitrate] = \begin{cases} 0 & , Nitrate >= 20 \\ (1 - \frac{Nitrate}{20}) \times Nitrate & , Nitrate < 20 \end{cases} \quad (3)$$

$$[Large\ Nitrate] = Nitrate - [Small\ Nitrate]$$

$$[Organic\ Mass] = OC_{2.5}$$

$$[Small\ \ Organic\ \ Mass] = \begin{cases} 0 & , [Organic\ \ Mass] >= 20 \\ (1 - \frac{[Organic\ \ Mass]}{20}) \times [Organic\ \ Mass] & , [Organic\ \ Mass] < 20 \end{cases}$$

$$[Large\ Organic\ Mass] = [Organic\ Mass] - [Small\ Organic\ Mass]$$

395 [*Elemental Carbon*]=$EC_{2.5}$

396 [*Fine Soil*]=$OIN_{2.5}$

397 [*Sea Salt*]=$CL_{2.5}$+$NA_{2.5}$

398 [*Coarse Mass*]=$SO4_{2.5\text{-}10}$+$NO3_{2.5\text{-}10}$+$NH4_{2.5\text{-}10}$+$OC_{2.5\text{-}10}$+

399 $EC_{2.5\text{-}10}$+$CL_{2.5\text{-}10}$+$NA_{2.5\text{-}10}$+$OIN_{2.5\text{-}10}$

400 The observation operators for $PM_{2.5}$ and PM_{10} were the sums of control
401 variables in the corresponding particle-size bin, that is,

402 $$PM_{2.5}=SO4_{2.5}+NO3_{2.5}+NH4_{2.5}+OC_{2.5}+EC_{2.5}+CL_{2.5}+NA_{2.5}+OIN_{2.5} \quad (4)$$

403 $$PM_{10}= PM_{2.5} + SO4_{2.5\text{-}10}+NO3_{2.5\text{-}10}+NH4_{2.5\text{-}10}+OC_{2.5\text{-}10}+EC_{2.5\text{-}10}+$$

404 $$CL_{2.5\text{-}10}+NA_{2.5\text{-}10}+OIN_{2.5\text{-}10} \quad (5)$$

405 The corresponding adjoint process on the operators for PM and AEC
406 were developed and passed the adjoint sensitivity test. For the adjoint test
407 method, please refer to Zou et al. (1997).

408 **2.6. DA and forecast experimental design and verification analysis method**

409 To analyze the effects of DA on aerosol analysis and forecasts, one
410 control experiment and three DA experiments were designed for a pollution
411 event that occurred from November 13 to 14, 2018 (Table 1). In the control
412 experiment, no chemical observation data were assimilated. Forecasts were
413 produced for a 36 h period, starting at 0000 UTC on November 13, 2018. In
414 the DA experiments, aerosol data were assimilated every hour for the DA
415 period of 0000–1200 UTC on November 13, 2018. Next, with the analysis
416 field obtained from the DA as the initial chemical field, forecasts were
417 performed for a 24 h period starting at 1200 UTC on November 13, 2018. For
418 the first DA cycle in each of the three DA experiments, the initial field of the

control experiment was used as the background field, the observation data for 0000 UTC on November 13, 2018 were assimilated, and a DA analysis field was generated. With this DA analysis field as the initial field at 0000 UTC, November 13, 2018 in the DA experiment, 1h forecasts were produced. The forecasts produced for 0100 UTC, November 13, 2018 were used as the background field for the second DA cycle. The process was repeated for 13 assimilation cycles. Thus, a DA analysis field for 1200 UTC, November 13, 2018 was generated. The effects of DA on forecast performance during the forecast comparison period from 1200 UTC, November 13, 2018 to 1200 UTC, November 14, 2018 was analyzed by comparing the forecast performance of the DA and control experiments. In the first DA experiment, PM data alone were assimilated (DA_PM). In the second DA experiment, the lidar data alone were assimilated (DA_Ext). In the third DA experiment, PM and lidar data were assimilated simultaneously (DA_PM_Ext). Furthermore, 0.25°×0.25° 6-h reanalysis data provided by the U.S. National Centers for Environmental Prediction (NCEP) were used as the meteorological field of the model.

Two metrics, the regional mean and root-mean-square error (RMSE), were used to evaluate simulation and forecast accuracy of the $PM_{2.5}$MC in the experiments. The closer the mean of the simulated values to the mean of the measurements and the smaller the RMSE, the higher the performance. Let M_i, O_i, N, $\overline{M}$, and $\overline{O}$ be the simulated value sample, the measured value sample, the number of samples, the mean of simulated values, and the mean of the measurements, respectively. The following summarizes the equations for calculating the metrics:

$$\overline{M} = \frac{1}{N}\sum_{i=1}^{N} M_i \quad (6)$$

$$\overline{O} = \frac{1}{N}\sum_{i=1}^{N} O_i \quad (7)$$

$$\mathrm{RMSE} = \sqrt{\frac{1}{N}\sum_{i=1}^{N}(M_i - O_i)^2} \quad (8)$$

3. Results

3.1. BESD and BEVCC

Under the same conditions, the larger the BESD, the larger the DA increment field (the difference between the "optimal" analysis field and the background field). Therefore, the structural pattern of the BESD significantly affected the distribution pattern of the DA increment field. The vertical BESD profiles of the 16 control variables are shown in Figure 2. The BESD differed significantly among the control variables. The seven control variables with the largest BESDs below the height of 1,000 m (corresponding to the 22nd layer of the model) in descending order of BESD were $OIN_{2.5\text{-}10}$, $NO3_{2.5}$, $OIN_{2.5}$, $NH4_{2.5}$, $SO4_{2.5}$, $OC_{2.5}$, and $EC_{2.5}$. As height increased, the BESD of each control variable decreased. The rates of decrease were the highest above the boundary layers at heights of 1,000–2,000 m (corresponding to the 20th–25th layers of the model).

The BEVCC matrix can spread the observation information contained in measurements around one model layer to nearby vertical layers. Therefore, even if the PM data are only available at the surface, there will still be increments of PM near the surface (in-air) after DA. Furthermore, even though the lidar AEC data are not available at the surface, assimilating lidar data can still correct the surface $PM_{2.5}$MC distribution. Figure 3 shows the BEVCC matrices of six control variables with relatively large BESDs ($OIN_{2.5\text{-}10}$, $NO3_{2.5}$, $OIN_{2.5}$, $NH4_{2.5}$, $SO4_{2.5}$, and $OC_{2.5}$). The BEVCCs of the six control variables share certain common characteristics. The correlation decreases as the interlayer spacing of the model increases. Each in-air layer is positively correlated with the surface layer, although the correlation decreases as height

increases. For $OIN_{2.5\text{-}10}$, the correlation coefficient between the surface and 10^{th} layers is 0.34, compared with 0.49-0.51 for other variables. This indicates that $OIN_{2.5\text{-}10}$ has a significantly weaker vertical correlation and hence DA increments of these particles settle more rapidly than the other variables do. This is mainly because coarse particles settle faster vertically than fine particles and are concentrated near the surface in larger quantities.

3.2. Analysis of the pollution process

Figure 4 shows the evolutionary process of the surface $PM_{2.5}$MC and the NCEP reanalysis surface wind field in the D02 region for the period from 0000 UTC, November 13, 2018 to 1200 UTC, November 14, 2018 (the time interval between Figure 4a, b, c, and d is 12 h). At 0000 UTC on November 13, 2018, the D02 region was predominantly controlled by a high-pressure circulation centered over Zibo. There was a clockwise wind field around the high-pressure center. Therefore, the northerlies (easterlies) east (south) of the high-pressure center brought clean air over the sealandward. As a result, the $PM_{2.5}$MCs over East China were relatively low. For example, the mean $PM_{2.5}$MC measured at the ground environmental monitoring stations in Nanjing was 41.8μg/m^3. There were relatively slow southerlies west and northwest of the high-pressure center, which led to favorable conditions for pollutant accumulation east of the Taihang Mountains and south of the Yan Mountains. As a result, North China was heavily polluted by $PM_{2.5}$. For example, the mean $PM_{2.5}$MCs in Beijing and Shijiazhuang were 122.7 and 149.3μg/m^3, respectively. In addition, within the D02 region, there was a northeast–southwest-trending cold front near Buyant-Ovoo–Bayan-Ovoo in Mongolia. As time passed (Figure 4b, c, and d), the high-pressure center gradually moved northeastward and reached near the eastern boundary of the D02 region by 1200 UTC, November 14, 2018 (Figure 4d). The cold front gradually moved southeastward and reached the

499 Chaoyang–Beijing–Taiyuan–Xi'an line by 1200 UTC, November 14, 2018
500 (Figure 4d). As the high-pressure center and the cold front moved, the level of
501 pollution in North China continued to rise, and pollution gradually expanded
502 northeastward to Chaoyang, southward to Zhengzhou, and westward to
503 Taiyuan. The level of pollution gradually increased in the Wei and Yellow
504 River Valleys east of Xi'an due to the dual action of advection by the
505 easterlies and the narrow terrain, while the $PM_{2.5}$MCs decreased considerably
506 with the passing of the cold front due to the good dispersion conditions. There
507 were no significant changes in the $PM_{2.5}$MCs in East China due to the
508 continuous impact of sea winds.

509 **3.3. Analysis of the direct effects of DA**

510 Figure 5 shows the AEC profile measurements, the AEC profiles in the
511 analysis fields of the control and DA experiments, and the simulated RH
512 profiles at four lidar stations at 0000 UTC, November 13, 2018, when the first
513 DA cycle was performed. The results of the control experiment were used as
514 the background field in the three DA experiments. Figures 5a, b, c, and d show
515 the results for Beijing, Shijiazhuang, Taiyuan, and Wuhu, respectively. As the
516 in-air RH profile (brown lines) below 1 km was basically consistent with that
517 of the surface RH, the vertical changes in the AEC values in this region were
518 only slightly affected by the RH. Thus, the AEC profiles were used to study
519 the vertical changes in the $PM_{2.5}$MC. For Beijing, the simulated AEC results
520 from the control experiment (blue lines) agreed with the lidar AEC
521 measurements well (Figure 5a—black lines). However, for Shijiazhuang and
522 Taiyuan, the simulation underestimated the empirical results (Figure 5b and
523 Figure 5c, respectively), particularly near the height of 100 m (the lowest
524 height of valid lidar data), while for Wuhu, it overestimated them (Figure 5d).

525 The DA increments of AEC values from the DA_PM, that is, the AEC

values obtained from the DA_PM experiment (green lines) minus those from the control experiment (blue lines), were negative for Beijing (Figure 5a), Taiyuan (Figure 5c), and Wuhu (Figure 5d) at the surface. They were also negative from the near-surface to a height of about 1000 m, although their absolute values were smaller than those at the surface. This is because the BEVCCs between each in-air layer and the surface layer were positive and decreased with height (Figure 3), so that the information contained in the surface PM MC measurements was spread to the air. However, the results of the adjustment of the AEC profiles were not always positive, because the aerosol bias of the control experiment at the surface was not always the same as it was in the atmosphere. Thus, they were overall positive for Beijing and Wuhu but negative for Taiyuan, reflecting the fact that the PM DA did not effectively account for the vertical aerosol distribution adjustment.

Compared to those from the DA_PM experiments, the AEC values from the DA_Ext experiments (purple lines) for Taiyuan (Figure 5c) at heights of approximately 100 and 700 m were significantly larger than those from the DA_PM experiment and were consistent with the measurements (black line), and those for Wuhu (Figure 5d) were very close to the measurements across the entire profile. This suggests that the AEC observation operator whose design was based on the IMPROVE equation effectively facilitated 3D variational assimilation of lidar AEC data. In addition, although lidar data were not available at the surface, the DA_Ext adjusted of the surface PM MCs, corrected the overestimation of surface PM2.5MCs in Beijing and Wuhu, but increased the overestimation of surface PM2.5MCs in Taiyuan. This is because the information contained in the in-air AEC was spread to the surface, while the aerosol bias of the control experiment in the air did not always match that at the surface.

The in-air AEC profiles obtained from the DA_PM_Ext experiment (red

554 lines) for the four cities almost coincided with those from the DA_Ext
555 experiments above 400 m. The near-surface AEC values obtained from the
556 DA_PM_Ext experiment for Beijing (Figure 5a), Taiyuan (Figure 5c), and
557 Wuhu (Figure 5d) almost coincided with those from the DA_PM experiment,
558 were between those from the DA_PM and DA_Ext experiments, and were
559 smaller than those from both the DA_PM and DA_Ext experiments. This
560 suggests that simultaneously assimilating the two types of data can fully
561 integrate their observation information and reflect their respective advantages,
562 thereby generating the most accurate analysis field.

563 Figure 6 shows the AEC profiles measured, simulated by the control
564 experiment, in the background fields and the analysis fields of the DA
565 experiments at four lidar stations at 1200 UTC, November 13, 2018. The time
566 of 1200 UTC, November 13, 2018 was the last time point of the DA period,
567 the starting time point of the forecast period, and the time point at which 13
568 DA cycles had elapsed. The background field for each of the three DA
569 experiments was generated during the continuous DA period, whereas the
570 results of the control experiment were obtained by a 12 h forecast starting at
571 0000 UTC, November 13, 2018. As a result, there was a significant difference
572 between the background fields of the three DA experiments and those of the
573 control experiment.

574 The DA increments of the AEC values from the DA_PM experiment
575 were significant below 1000 m (green lines). These adjustments corrected the
576 near-surface overestimation of the AEC values for the four cities in the control
577 experiment, however, increased the underestimation for Taiyuan at heights of
578 120–400 m (Figure 6c) and overestimation for Wuhu above 400 m (Figure 6d).
579 Additionally, it is worth noting that there were small direct DA increments
580 generated in the DA_PM experiment at this time point. This means that for the
581 surface PM DA, a DA period of 11 h or less was sufficient to effectively

adjust aerosol distribution in this experiment. This may because aerosols were primarily concentrated near the surface and surface PM data covered a wide area and had a high spatial resolution, thus, surface PM data measured at a few time points contained the main aerosol distribution information for the whole region.

Compared to the DA_PM experiment, the DA_Ext experiment (purple lines) reflected the advantages of adjusting the vertical aerosol distribution. The overestimations for Beijing above 300 m (Figure 6a), Taiyuan above 600 m (Figure 6c), and Wuhu below 400 m (Figure 6d) in the control experiment were effectively corrected. The rapid decrease in the AEC from the surface to a height of 1,000 m over Beijing (Figure 6a) and the maximum-AEC layer at a height of 1,300 m over Wuhu (Figure 6d) were accurately reproduced by the DA_Ext experiment. However, the near-surface overestimation for Taiyuan (Figure 6c) increased. Moreover, the direct DA increments generated in the DA_Ext experiment at this time point remained notable. This suggests that the background field errors at each lidar station at 1200 UTC remained relatively large, even after the continuous DA period. To improve the effects of the DA, it was necessary to increase the length of the continuous DA period. This may have been due to the limited number of lidars and the fact that the lidars were relatively far apart from one another. Thus, the simulation error for the region upstream of a lidar was difficult to correct through DA and affected the lidar location due to the effects of advection at the next time point. In addition, because the 1200UTC (2000LST) was only 2-3 h after sunset, so large changes of PM concentration profile may occur due to large changes in the PBLH after sunset.

Figure 7 shows the surface $PM_{2.5}$ MC measurements, the surface $PM_{2.5}$MCs of the initial field of the control experiment and their biases, and the inverse DA increments of $PM_{2.5}$MCs from the DA experiments, that is, the

610 $PM_{2.5}$MCs obtained from the control experiment minus those from the DA
611 experiments at 1200UTC, November 13, 2018. The measurements (Figure 7a)
612 showed that the $PM_{2.5}$MCs were relatively high in North China, with a heavily
613 polluted zone in the Beijing–Shijiazhuang–Zhengzhou region, while the
614 $PM_{2.5}$MCs were relatively low surrounding North China. The control
615 experiment (Figure 7b) successfully simulated regions with relatively high and
616 low $PM_{2.5}$MCs. However, the $PM_{2.5}$MCs were overestimated for most stations
617 in D02 (Figure 7c), especially in the Beijing–Shijiazhuang–Zhengzhou region,
618 and underestimated for stations near Chaoyang.

619 The inverse DA increments of the PM2.5MCs of the DA_PM experiment
620 (Figure 7d) were relatively consistent with the bias of the control experiment
621 (Figure 7c), indicating that the overestimation for most regions and the
622 underestimation for some regions in the initial field of the control experiment
623 were corrected by the PM DA. The inverse DA increments of the PM2.5MCs
624 of DA_Ext (Figure 7e) were significant in the regions surrounding and
625 downstream of the five lidar stations. In addition, certain DA increments were
626 also present in regions far away from the lidar stations. This indicates that
627 long-term continuous lidar AEC DA can affect a relatively large area. Overall,
628 the DA_Ext corrects the overestimation for most stations and underestimation
629 for a few stations in the control experiment. However, the DA_Ext increments
630 were smaller than the DA_PM increments in terms of horizontal spatial range
631 and absolute values. This is mainly because there are relatively few lidars, and
632 these lidars cover a limited spatial area. It is worth noting that DA_Ext yields
633 a negative effect for northern Beijing and the region around Taiyuan, a result
634 which will be discussed later in Chapter 4. The inverse DA increments of
635 PM2.5MCs of DA_PM_Ext (Figure 7f) were relatively consistent with those
636 of the DA_PM (Figure 7c). This is mainly because the quantity and spatial
637 coverage of the PM data were larger and more complete than those of the lidar

638 data. As a result, the DA increments of the surface PM2.5MCs originated
639 primarily from the observation information contained in the PM data. Because
640 the AEC profiles of the DA_PM_Ext almost coincided with those of the
641 DA_Ext above 400 m (Figure 5), the DA_PM_Ext reflected the 3D spatial
642 distribution pattern of the aerosols most accurately.

643 **3.4. Effects of DA on the forecast performance for surface $PM_{2.5}$MCs**

644 In this section, the forecast performances of the DAs for surface $PM_{2.5}$
645 are evaluated based on measurements that cover most of the D02 region.

646 Figure 8 shows the variation of the regional mean of the $PM_{2.5}$MC over
647 time from the four experiments. The regional mean of the $PM_{2.5}$MC (black
648 line) exhibited a notable diurnal pattern. Two notable minimum $PM_{2.5}$MC
649 values (69.1 and 77.9μg/m^3) appeared at 0800 UTC (1600 local time) on
650 November 13 and November 14, 2018, respectively. High $PM_{2.5}$MCs appeared
651 between 1300 UTC, November 13, 2018 and 0200 UTC, November 14, 2018
652 (from night to morning), with a maximum $PM_{2.5}$MC of 96.0μg/m^3. Meanwhile,
653 there was a relative minimum $PM_{2.5}$MC (87.0μg/m^3) appearing at 2200 UTC
654 on November 13, 2018 (around dawn local time) during the high-$PM_{2.5}$-MC
655 period.

656 The control experiment (blue line) simulated the periodic variation
657 pattern of the mean $PM_{2.5}$MC but significantly overestimated the value of this
658 parameter during the entire forecast period. The mean $PM_{2.5}$MC of the control
659 experiment at the initial time for the forecast period (1200 UTC, November 13,
660 2018) was 128.6μg/m^3, which is 36.3μg/m^3 (39.3%) larger than that of the
661 measurements (92.3μg/m^3). The DA_PM (green line, which almost coincides
662 with the red line) significantly reduced the overestimation of the control
663 experiment, with a mean $PM_{2.5}$MC of 91.4μg/m^3 that is 0.9μg/m^3 (1.0%) lower
664 than the measurement. As a result of the decrease in the MC levels in the

initial field, the $PM_{2.5}$MC forecasts of the DA_PM were significantly lower than those of the control experiment during the entire forecast period. This suggests that the overestimation of the initial field is the primary cause of the overestimated forecasts of the control experiment. The overestimation of the control experiment at the initial time point was reduced by the DA_Ext (purple line) from 36.3μg/m^3 (39.3%) to 20.5μg/m^3 (22.2%), which improved the forecast performance significantly (even though there were only five lidars within the region). There was no significant difference between the results of the DA_PM_Ext (red line) and DA_PM (green line) at the surface. This suggests that in these experiments, after DA of surface PM data, the DA of lidar data did not significantly affect the surface $PM_{2.5}$MC levels. There are two reasons for this. The PM data set was far larger than the lidar data set in terms of quantity and spatial coverage. In addition, after surface PM DA, lidar DA mainly directly adjusted the AMC values not at surface but in-air and hence affected the surface AMC forecasts only indirectly, via processes such as settling. However, in this simulation process, the surface AMC levels remained relatively high, while the vertical air movement was weak due to the relatively stable meteorological conditions, particularly in the heavily polluted zone. Therefore, the effects of the lidar DA on the surface $PM_{2.5}$MCs are far smaller after the surface PM DA.

Figure 9 shows the variation in the RMSE of surface $PM_{2.5}$MC forecasts over time. The RMSEs for simulations and forecasts were relatively large (small) when the mean $PM_{2.5}$MCs were relatively high (low) (Figure 8). The RMSE in the control experiment was 59.6μg/m^3 at the initial time for the forecast period (1200 UTC, November 13, 2018) and fluctuated between 44.5 and 67.1μg/m^3 instead of linearly increasing or decreasing throughout the forecast period. The RMSEs in the DA_PM (green line), DA_Ext (purple line), and DA_PM_Ext (red line) experiments at the initial time point were 21.0,

693 49.1, and 21.2μg/m^3, respectively, which were 38.6μg/m^3 (64.8%), 10.5μg/m^3
694 (17.6%), and 38.4μg/m^3 (64.4%) lower than that of the control experiment.
695 Owing to the optimized initial field, the RMSE of the forecasts of each of the
696 DA experiments was lower than that of the control experiment during the
697 forecast period. For the 24th forecast hour, the RMSEs of the forecasts of the
698 Da_PM, Da_Ext, and DA_PM_Ext were 6.1μg/m^3 (11.8%), 1.5μg/m^3 (2.9%),
699 and 6.5μg/m^3 (12.6%) smaller than that of the control experiment, respectively.
700 This suggests that the optimization of the initial field has a lasting (more than
701 24 h in all cases) positive effect on model forecasts. It is worth noting that
702 while there are very few lidar stations, the results of the DA_Ext experiment
703 were still better than those of the control experiment, and the results of the
704 DA_PM_Ext experiment were also slightly better than those of the DA_PM
705 experiment. This indicates that even in relatively low quantities, lidar data still
706 improve the forecast performance of the model. As lidar data become
707 increasingly rich and provide more vertical and horizontal aerosol distribution
708 information in the future, lidar DA will further improve $PM_{2.5}$MC forecasts.

709 **4. Discussion**

710 DA_Ext had a negative effect on the surface $PM_{2.5}$ MC distributions for
711 regions around Taiyuan and northern Beijing (Figure 7e). For Taiyuan, the
712 cause of the negative effect was similar to that responsible for the results
713 shown in Figure 5, that is, the information contained in the in-air AEC was
714 spread to the surface by DA_Ext. However, the AEC showed an
715 underestimation bias of the control experiment at a height of 100 m, while the
716 PM MC measurements showed an overestimation bias at the surface. There
717 are two reasons for the differences between the bias of the control experiment
718 in-air and at surface, as reflected by the AEC and PM MC measurements. First,
719 it is not abnormal for the simulation error of the model to differ in the vertical

direction due to the complex evolution mechanism of aerosols, which we do not discuss here. Second, the $PM_{2.5}$MCs measured at 1200 UTC, November 13, 2018 at three ground environmental monitoring stations within 6 km of the Taiyuan lidar station were 80.0 μg/m^3, 137.0 μg/m^3, and 146.0 μg/m^3, respectively, indicating a large horizontal gradient of AMC and PM MC around the Taiyuan lidar station. Therefore, the observation information contained in the lidar profile did not represent the spatial distribution well and differed significantly from that contained in the PM data nearby. This suggests that the spatial representation of lidar data could significantly affect the impact of the lidar AEC DA. In addition, the vertical resolution of the lidar data (smaller than 15 m) is far smaller than the spacing between adjacent height layers of the model. As a result, the representative spatial scale of the original lidar data does not match the resolution of the model. To improve the accuracy of the horizontal spatial representativeness of the lidar data, at each time point, the lidar AEC profile was based on hourly averaged lidar data (from the previous hour). The vertical spatial representativeness of the data was improved by smoothing over 30 m in the vertical direction. However, the time-averaged lidar data represented observation information for a certain area downstream of the wind field. These errors need to be addressed in subsequent studies. Moreover, the selection of a time-averaging period and vertical smoothing length also requires further investigation.

For northern Beijing, the underestimation resulted primarily from the notable Beijing lidar overestimation, whereas the overestimation was relatively small in northern Beijing, the downstream region of the Beijing lidar. In addition, there was even underestimation in some of the PM measurement stations north of Beijing (Figure 7c). Therefore, the downstream transference of lidar DA information from Beijing lidar location to northern Beijing caused the underestimation in the continuous DA results. The most direct and

748 effective measure for addressing this problem is to increase the number of
749 lidars and the coverage of the lidar network. This measure will ensure that the
750 simulation bias for the simulation region will be more comprehensively
751 captured. However, lidar detection requires large amounts of labor and
752 financial resources. Therefore, it is difficult to arrange lidar stations as densely
753 as ground environmental monitoring stations. A relatively feasible method is
754 to set a relatively small number of lidars in regions with a relatively uniform
755 simulation bias and set dense lidars in regions where the simulation bias
756 changes significantly. This will make it possible to use a limited number of
757 lidars to capture more useful information. Thus, studying the temporal and
758 spatial distribution of model simulation bias can provide a useful reference for
759 the future arrangement and planning of the lidar stations. This merits further
760 investigation.

761 The AEC observation operator used in this study was designed based on
762 the IMPROVE equation, with parameters such as the hygroscopicity
763 coefficient set to values reported in previous studies. On the one hand, datasets
764 from which the IMPROVE parameters were determined in previous studies
765 were measured in specific regions and near the ground. The verification of the
766 IMPROVE parameters had not been thoroughly conducted for the locations
767 where lidar data were provided. Therefore, there may have been different
768 biases between the Mie algorithm and the IMPROVE algorithm in different
769 regions, inducing inconsistent assimilation performance. Additionally, the
770 values of the coefficients in the IMPROVE equation were determined by
771 statistical analysis of extensive data. This dictated that these coefficients
772 represented average levels under certain pollution and humidity conditions.
773 There may be certain biases in these coefficients when applied to a specific
774 observation event. These biases will accumulate and amplify during the
775 calculation of the forward and adjoint processes of the observation operator,

776 resulting in a negative effect DA effect. Hence, another issue needing to be
777 addressed is how to effectively evaluate the applicability of the IMPROVE
778 equation and more accurately adjust its coefficients.

779 **5. Conclusions**

780 In this study, an observation operator and its adjoint for the AEC DA
781 were designed based on the IMPROVE equation, and a 3-DVAR DA system
782 was developed for lidar AEC data and surface AMC data for the
783 MOSAIC-4bin chemical scheme in the WRF–Chem model. Three DA
784 experiments (i.e., a $PM_{2.5}$(PM_{10}) DA experiment, a lidar AEC DA experiment,
785 and a simultaneous $PM_{2.5}$(PM_{10}) and lidar AEC DA experiment) were
786 conducted based on AEC profiles captured by five lidars (located in Beijing,
787 Shijiazhuang, Taiyuan, Xuzhou, and Wuhu) as well as $PM_{2.5}$ and PM_{10}
788 measurements taken at over 1,500 ground environmental monitoring stations
789 across China in the period from 0000 to 1200 UTC, November 13, 2018. A
790 comparison with the control experiment involving no DA found that the
791 3-DVAR DA system was effective at assimilating lidar AEC data. While there
792 were only five lidars within the simulation region (approximately 2.33 million
793 km^2 in size), assimilating AEC data alone was still found to effectively
794 improve the accuracy of the initial field, hence improving the forecast
795 performance for $PM_{2.5}$ for more than 24 h. The lidar AEC DA can reduce the
796 RMSE of the surface $PM_{2.5}$MC in the initial field of the model by 10.5μg/m^3
797 (17.6%). In addition, a 38.4μg/m^3 (64.4%) reduction occurred when the
798 $PM_{2.5}$(PM_{10}) and lidar AEC data were assimilated simultaneously. The RMSEs
799 of the forecasted surface $PM_{2.5}$MC 24 h after the DA period in the three DA
800 experiments were reduced by 6.1μg/m^3 (11.8%), 1.5μg/m^3 (2.9%), and
801 6.5μg/m^3 (12.6%), respectively. Lidar AEC DA was advantageous for
802 improving the accuracy of the vertical $PM_{2.5}$MC profile. Surface $PM_{2.5}$(PM_{10})

DA was advantageous for optimizing the near-surface $PM_{2.5}$MC distribution. Simultaneous lidar AEC and surface $PM_{2.5}$(PM_{10}) DA effectively integrated their observation information to generate a more accurate 3D aerosol analysis field.

Code and data availability: The WRF-Chem model source code can be downloaded at the WRF model downloadpage (https://www2.mmm.ucar.edu/wrf/users/download/get_source.html). This 3-DVAR data assimilation system was developed by the authors. The code of this system can be obtained on request from the corresponding author (ywlx_1987@163.com and zzlqxxy@163.com). Aerosol lidar data can be obtained on request from the first author (13270805867@163.com).

Author contribution: Yanfei Liang performed numerical experiments, data analysis and wrote the initial manuscript. Yanfei Liang, Zengliang Zang and Wei You developed the 3-DVAR data assimilation system, designed this study and revised the manuscript. Zengliang Zang supervised the project of development. Dong Liu provided the lidar observation data in four sites. All the authors continuously discussed the 3-DVAR system development and the results of the manuscript.

Competing interests: The authors declare that they have no conflict of interest.

Acknowledgments

This research was primarily supported by the National Key Research and Development Program of China (Grant No.2017YFC1501700), the National Natural Science Foundation of China (Grant No.41775123 and No.41805092).

We thank the China National Environmental Monitoring Center (CNEMC) for providing $PM_{2.5}$ and PM_{10} data through the website (http://www.cnemc.cn/).

References:

Bannister, R. N.: A review of operational methods of variational and ensemble‐variational data assimilation, Q. J. Roy. Meteor. Soc., 143, 607-633, https://doi.org/10.1002/qj.2982, 2017.

Baraskar, A., Bhushan, M., Venkataraman, C., Cherian, R.: An offline constrained data assimilation technique for aerosols: Improving GCM simulations over South Asia using observations from two satellite sensors, Atmos. Environ., 132, 36-48, https://doi.org/ 10.1016/j.atmosenv.2016.02.026, 2016.

Benedetti, A., Morcrette, J. J., Boucher, Dethof, O., Engelen, R. J., Fisher, M., Flentje, H., Huneeus, N., Jones, L., Kaiser, J. W., Kinne,S., Mangold, A., Razinger, M., Simmons, A. J., Suttie, M.: Aerosol analysis and forecast in the European Centre for Medium-Range Weather Forecasts Integrated Forecast System: 2. Data assimilation, J. Geophys. Res., 114, D13205, https://doi.org/ 10.1029/2008JD011115, 2009.

Burton, S. P., Ferrare, R. A., Hostetler, C. A., Hair, J. W., Kittaka, C., Vaughan, M. A., Obland, M. D., Rogers, R. R., Cook, A. L., Harper, D. B., Remer, L. A.: Using airborne high spectral resolution lidar data to evaluate combined active plus passive retrievals of aerosol extinction profiles, J. Geophys. Res.-Atmos., 115, D4, https://doi.org/ 10.1029/2009JD012130, 2010.

Cao, J. J., Wang, Q. Y., Chow, J. C., Watson, J. G., Tie, X. X., Shen, Z. X., Wang, P., An, Z. S.: Impacts of aerosol compositions on visibility impairment in Xi'an, China, Atmos. Environ., 59, 559–566, https://doi.org/10.1016/j.atmosenv.2012.05.036, 2012.

Cao, J. J., Shen, Z. X., Chow, J. C., Watson, J. G., Lee, S. C., Tie, X. X., Ho, K. F., Wang, G. H., Han, Y. M.: Winter and Summer PM2.5 Chemical Compositions in Fourteen Chinese Cities, J. Air. Waste. Manage., 62, 1214-1226, https://doi.org/10.1080/10962247.2012.701193, 2012.

853 Carmichael, G. R., Sandu, A., Chai, T., Daescu, D. N., Constantinescu, E. M., Tang, Y.: Predicting
854 air quality: Improvements through advanced methods to integrate models and measurements, J.
855 Comput. Phys., 227, 3540-3571, https://doi.org/10.1016/j.jcp.2007.02.024, 2008.

856 Cheng, X. H., Liu, Y. L., Xu, X. D., You, W., Zang, Z. Z., Gao, L. N., Chen, Y. B., Su, D. B., Yan, P.:
857 Lidar data assimilation method based on CRTM and WRF-Chem models and its application in
858 PM2.5 forecasts in Beijing, Sci. Total. Environ., 682, 541-552,
859 https://doi.org/10.1016/j.scitotenv.2019.05.186, 2019.

860 Chen, Y., Li, F. F., Shao, N., Wang, X. P., Wang, Y. M., Hu, X. Y., Wang, X.: Aerosol Lidar
861 Intercomparison in the Framework of the MEMO Project. 1. Lidar Self Calibration and 1st
862 Comparison Observation Calibration Based on Statistical Analysis Method, in: 2019
863 International Conference on Meteorology Observations (ICMO), Chengdu, China, 28-31
864 December 2019, 1-5, https://doi.org/10.1109/ICMO49322.2019.9026086, 2019.

865 Chen, Z. J., Zhang, J. S., Zhang, T. S., Liu, W. Q., Liu, J. G.: Haze observations by simultaneous
866 lidar and WPS in Beijing before and during APEC, 2014, Sci. China. Chem., 58, 1385–1392,
867 https://doi.org/10.1007/s11426-015-5467-x, 2015.

868 Ganguly, D., Ginoux, P., Ramaswamy, V., Dubovik, O., Welton, J., Reid, E. A., Holben, B. N.:
869 Inferring the composition and concentration of aerosols by combining AERONET and
870 MPLNET data: Comparison with other measurements and utilization to evaluate GCM output,
871 J. Geophys. Res.-Atmos. 114, D16, https://doi.org/ 10.1029/2009JD011895, 2009.

872 Fernald, F. G.: Analysis of atmospheric lidar observations: some comments, Appl. Optics., 23, 652–
873 653, https://doi.org/10.1364/AO.23.000652, 1984.

874 Gordon T. D., Prenni A. J., Renfro J. R., McClure, E., Hicks, B., Onasch, T. B., Freedman, A.,
875 McMeeking, G. R., Chen, P.: Open-path, closed-path and reconstructed aerosol extinction at a
876 rural site, J. Air. Waste. Manage., 68, 824-835,
877 https://doi.org/10.1080/10962247.2018.1452801, 2018.

878 Haywood, J., and O. Boucher.: Estimates of the direct and indirect radiative forcing due to

879 tropospheric aerosols: A review, Rev. Geophys., 38, 513–543,
880 https://doi.org/10.1029/1999RG000078, 2000.

881 Jiang, Z. Q., Liu, Z. Q., Wang, T. J., Schwartz, C. S., Lin, H. C., Jiang, F.: Probing into the impact of
882 3-DVAR assimilation of surface PM10 observations over China using process analysis, J.
883 Geophys. Res.-Atmos., 118, 6738-6749, https://doi.org/10.1002/jgrd.50495, 2013.

884 Kahnert, M.: Variational data analysis of aerosol species in a regional CTM: background error
885 covariance constraint and aerosol optical observation operators, Tellus B, 60, 753-770,
886 https://doi.org/10.1111/j.1600-0889.2008.00377.x, 2008.

887 Kim, Y. J., Kim, K. W., Kim, S. D., Lee, B. K., Han, J. S.: Fine particulate matter characteristics and
888 its impact on visibility impairment at two urban sites in Korea: Seoul and Incheon, Atmos.
889 Environ., 40(supp-S2), 593–605, https://doi.org/10.1016/j.atmosenv.2005.11.076, 2006.

890 Li, Z. J., Zang, Z. L., Li, Q. B., Chao, Y., Chen, D., Ye, Z., Liu, Y., Liou, K. N.: A three-dimensional
891 variational data assimilation system for multiple aerosol species with WRF/Chem and an
892 application to PM2.5 prediction, Atmos. Chem. Phys., 13, 4265-4278,
893 https://doi.org/10.5194/acp-13-4265-2013, 2013.

894 Liu, Q. H., Weng, F. Z.: Advanced doubling-adding method for radiative transfer in planetary
895 atmosphere, J. Atmos. Sci., 63, 3459–3465, https://doi.org/10.1175/JAS3808.1, 2006.

896 Liu, Z., Q. Liu, Q. H., Lin, H. C., Schwartz, C. S., Lee, Y. H., Wang, T. J.: Three-dimensional
897 variational assimilationof MODIS aerosol optical depth: Implementation and application to a
898 dust storm over East Asia, J. Geophys. Res.-Atmos., 116, D23206,
899 https://doi.org/10.1029/2011JD016159, 2011.

900 Milroy, C., Martucci, G., Lolli, S., Loaer, S., Sauvage, L., Xueref-Remy, I., Lavrič, J. V., Ciais, P.,
901 O'Dowd, C.D.: On the ability of pseudo-operational ground-based light detection and ranging
902 (LIDAR) sensors to determine boundary-layer structure: intercomparison and comparison with
903 in-situ radiosounding, Atmos. Meas. Tech. Discuss., 4, 563–597,
904 https://doi.org/10.5194/amtd-4-563-2011, 2011.

905 Lowenthal, D. H., Kumar, N.: PM2.5 Mass and Light Extinction Reconstruction in IMPROVE, J.
906 Air. Waste. Manage., 53, 1109-1120, https://doi.org/10.1080/10473289.2003.10466264, 2003.

907 Matthais, V., Freudenthaler, V., Amodeo, A., Balin, I., Balis, D., Bösenberg, J., Chaikovsky, A.,
908 Chourdakis, G., Comeron, A., Delaval, A., Tomasi, F. D., Eixmann, R., Hågård, A., Komguem,
909 L., Kreipl, S., Matthey, R., Rizi, V., Rodrigues, J. A., Wandinger, U., and Wang, X.: Aerosol
910 lidar intercomparison in the framework of the EARLINET project. 1. Instruments, Appl.
911 Optics., 43, 961-976, https://doi.org/10.1364/AO.43.000961, 2004.

912 Niu, T., Gong, S. L., Zhu, G. F., Liu, H. L., Hu, X. Q., Zhou, C. H., Wang, Y. Q.: Data assimilation
913 of dust aerosol observations for the CUACE/dust forecasting system, Atmos. Chem. Phys., 7,
914 3473–3482, https://doi.org/10.5194/acpd-7-8309-2007, 2008.

915 Parrish, D. F., and Derber, J. C.: The national meteorological center's spectral
916 statistical-interpolation analysis system, Mon. Wea. Rev., 120, 1747–1763,
917 https://doi.org/10.1175/1520-0493(1992)120<1747:TNMCSS>2.0.co;2, 1992.

918 Peng, Z., Liu, Z. Q., Chen, D. , Ban, J. M.: Improving PM2.5 forecast over China by the joint
919 adjustment of initial conditions and source emissions with an ensemble Kalman filter, Atmos.
920 Chem. Phys., 17, 4837-4855, https://doi.org/10.5194/acp-2016-732, 2016.

921 Pitchford, M., Maim, W., Schichtel, B., Kumar, N., Lowenthal, D., Hand, J.: Revised algorithm for
922 estimating light extinction from IMPROVE particle speciation data, J. Air. Waste. Manage., 57,
923 1326-1336, https://doi.org/10.3155/1047-3289.57.11.1326, 2007.

924 Raut, J. C., Chazette, P.: Assessment of vertically-resolved PM10 from mobile lidar observations,
925 Atmos. Chem. Phys., 9, 8617-8638, https://doi.org/10.5194/acpd-9-13475-2009, 2009.

926 Roy, B., Mathur, R., Gilliland, A. B., Howard, S. C.: A comparison of CMAQ-based aerosol
927 properties with IMPROVE, MODIS, and AERONET data, J. Geophys. Res., 112, D14,
928 https://doi.org/10.1029/2006JD008085, 2007.

929 Ryan, P. A., Lowenthal, D., Kumar, N.: Improved Light Extinction Reconstruction in Interagency

930 Monitoring of Protected Visual Environments, J. Air. Waste. Manage., 55, 1751-1759,
931 https://doi.org/ 10.1080/10473289.2005.10464768, 2005.

932 Sandu, A., Chai, T.: Chemical Data Assimilation—An Overview, Atmosphere-Basel, 2, 426-463,
933 https://doi.org/10.3390/atmos2030426, 2011.

934 Sekiyama, T. T., Tanaka, T. Y., Shimizu, A., Miyoshi, T.: Data assimilation of CALIPSO aerosol
935 observations, Atmos. Chem. Phys., 10, 39–49, https://doi.org/10.5194/acp-10-39-2010, 2010.

936 Schwartz, C. S., Liu, Z. Q., Lin, H. C., McKeen, S. A.: Simultaneous three-dimensional variational
937 assimilation of surface fine particulate matter and MODIS aerosol optical depth, J. Geophys.
938 Res.-Atmos., 117, D13, https://doi.org/10.5194/acp-10-39-2010, 2012.

939 Sugimoto, N., Matsui, I., Shimizu, A., Nishizawa, T., Yoon, S. C.: Lidar network observations of
940 tropospheric aerosols, SPIE, 7153, https://doi.org/10.1117/12.806540, 2008.

941 Sugimoto, N., and Huang Z. W.: Lidar methods for observing mineral dust, J. Meteor. Res., 28,
942 173–184, https://doi.org/10.1007/s13351-014-3068-9, 2014.

943 Tang, Y. H., Pagowski, M., Chai, T. F., Pan, L., Lee1, P., Baker, B., Kumar, R., Monache, L. D.,
944 Tong, D., Kim, H. C.: A case study of aerosol data assimilation with the Community
945 Multi-scale Air Quality Model over the contiguous United States using 3D-Var and optimal
946 interpolation methods, Geosci. Model. Dev., 10, 4743–4758,
947 https://doi.org/10.5194/gmd-10-4743-2017, 2017.

948 Tao, J., Ho, K. F., Chen, L., Zhu, L., Han, J., Xu, Z.: Effect of chemical composition of PM2.5 on
949 visibility in Guangzhou, China, 2007 spring, Particuology, 7, 68–75, https://doi.org/
950 10.1016/j.partic.2008.11.002, 2009.

951 Tao, J., Cao J. J., Zhang, R. J., Zhu, L. H., Zang, T., Shi, S., Chan, C. Y.: Reconstructed light
952 extinction coefficients using chemical compositions of PM2.5 in winter in urban Guangzhou,
953 China, Adv. Atmos. Sci., 29, 359-368, https://doi.org/10.1007/s00376-011-1045-0, 2012.

954 Tao, J., Zhang, L. M., Ho, K. F., Zhang, R. J., Lin, Z. J., Zhang, Z. S., Lin, M., Cao, J. J., Liu, S. X.,

955 Wang, G. H.: Impact of PM2.5 chemcial compositions on aerosol light scattering in
956 Guangzhou-the largest megacity in South China, Atmos. Res., 135–136, 48–58,
957 https://doi.org/10.1016/j.atmosres.2013.08.015, 2014.

958 Tesche, M., Ansmann, A., Müller, D., Althausen, D., Engelman, R..: Particle backscatter, extinction,
959 and lidar ratio profiling with Raman lidar in south and north China, Appl. Optics., 46,
960 6302–6308, https://doi.org/10.1364/AO.46.006302, 2007.

961 Tombette, M., Mallet, V., Sportisse, B.: PM10 data assimilation over Europe with the optimal
962 interpolation method, Atmos. Chem. Phys., 9, 57-70, https://doi.org/ 10.5194/acp-9-57-2009,
963 2008.

964 Wang D, You W, Zang Z, Pan X, He H, Liang Y.: A three-dimensional variational data assimilation
965 system for a size-resolved aerosol model: Implementation and application for particulate
966 matter and gaseous pollutant forecasts across China, Sci. China. Earth. Sci., 63, 1366-1380,
967 https://doi.org/10.1007/s11430-019-9601-4, 2020.

968 Wang, Y., Sartelet, K. N., Bocquet, M., Chazette, P.: Assimilation of ground versus lidar
969 observations for PM10 forecasting, Atmos. Chem. Phys., 13, 269-283,
970 https://doi.org/10.5194/acpd-12-23291-2012, 2013.

971 Wang, Y., Sartelet, K. N., Bocquet, M., Chazette, P.: Modelling and assimilation of lidar signals
972 over Greater Paris during the MEGAPOLI summer campaign, Atmos. Chem. Phys., 14,
973 3511-3532, https://doi.org/10.5194/acp-14-3511-2014, 2014a.

974 Wang, Y., Sartelet, K. N., Bocquet, M., Chazette, P., Sicard, M., Amico, G. D., Léon, J. F.,
975 Arboledas-Arboledas, L., Amodeo, A., Augustin, P., Bach, J., Belegante, L., Binietoglou, I.,
976 Bush, X., Comerón, A., Delbarre, H., García-Vízcaino, D., Guerrero-Rascado, J. L., Hervo, M.,
977 Iarlori, M., Kokkalis, P., Lange, D., Molero, F., Montoux, N., Muñoz, A., Muñoz, C., Nicolae,
978 D., Papayannis, A., Pappalardo, G., Preissler, J., Rizi, V., Rocadenbosch4, F., Sellegri, K.,
979 Wagner, F., Dulac, F.: Assimilation of lidar signals: application to aerosol forecasting in the
980 western Mediterranean basin, Atmos. Chem. Phys., 14, 134-138,

https://doi.org/10.5194/acp-14-12031-2014, 2014b.

Wiscombe, W. J.: Improved MIE scattering algorithms, Appl. Optics., 1980, 19, 1505-1509, https://doi.org/10.1364/AO.19.001505, 1980.

Wu, J. B., Xu, J. M., Pagowski, M., Geng, F. H., Gu, S. Q., Zhou, G. Q., Xie, Y., Yu, Z. Q.: Modeling study of a severe aerosol pollution event in December 2013 over Shanghai China:An application of chemical data assimilation, Particuology, 20, 41-51, https://doi.org/ 10.1016/j.partic.2014.10.008, 2015.

Xia, X. L., Min, J. Z., Shen, F. F., Wang, Y. B., Yang, C.: Aerosol data assimilation using data from Fengyun-3A and MODIS: application to a dust storm over East Asia in 2011, Adv. Atmos. Sci., 36, 1–14, https://doi.org/10.1007/s00376-018-8075-9, 2019.

Young, S. A., Vaughan, M. A.: The retrieval of profiles of particulate extinction from Cloud-Aerosol Lidar Infrared Pathfinder Satellite Observations (CALIPSO) data: Algorithm description, J. Atmos. Ocean. Tech., 26, 1105–1119, https://doi.org/ 10.1175/2008JTECHA1221.1, 2009.

Yumimoto, K., Murakami, H., Tanaka, T. Y., Sekiyama, T. T., Ogi, A., Maki, T.: Forecasting of Asian dust storm that occurred on May 10–13, 2011, using an ensemble-based data assimilation system, Particuology, 28, 121-130, https://doi.org/10.1016/j.partic.2015.09.001, 2015.

Yumimoto, K, Nagao, T. M., Kikuchi, M., Sekiyama, T. T., Murakami, H., Tanaka, T. Y., Ogi, A., Irie, H., Khatri, P., Okumura, H., Arai, K., Morino, I., Uchino, O., Maki, T.: Aerosol data assimilation using data from Himawari-8, a next-generation geostationary meteorological satellite, Geophys. Res. Lett., 43, 5886-5894, https://doi.org/10.1002/2016GL069298, 2016.

Zhang, S., Zhou, Z. M., Ye, C. L., Shi, J. B., Wang, P., Liu, D.: Analysis of a Pollution Transmission Process in Hefei City Based on Mobile Lidar, in: EPJ Web Conf. 237 02006(2020), https://doi.org/10.1051/epjconf/202023702006, 2020.

Zang, Z. Z., Li, Z. J., Pan, X. B., Hao, Z. L., You, W.: Aerosol data assimilation and forecasting

experiments using aircraft and surface observations during CalNex, Tellus B, 68, 1-14, https://doi.org/10.3402/tellusb.v68.29812, 2016.

Zou, X., Vandenberghe, F., Pondeca, M., Kuo, Y. H.: Introduction to Adjoint Techniques and the MM5 Adjoint Modeling System, NCAR Technical Note NCAR/TN-435-STR 122, https://doi.org/10.5065/D6F18WNM, 1997.

Table 1. Numerical experiment schemes

Experiment	Assimilated data	Assimilation region	DA period	Forecast comparison period
Control	N/A	N/A	N/A	11.13 12:00 –11.14 12:00
DA_PM	$PM_{2.5}$+PM_{10}	D01/D02	11.13 00:00 –11.13 12:00	11.13 12:00 –11.14 12:00
DA_Ext	Ext	D01/D02	11.13 00:00 –11.13 12:00	11.13 12:00 –11.14 12:00
DA_PM_Ext	$PM_{2.5}$+PM_{10}+Ext	D01/D02	11.13 00:00 –11.13 12:00	11.13 12:00 –11.14 12:00

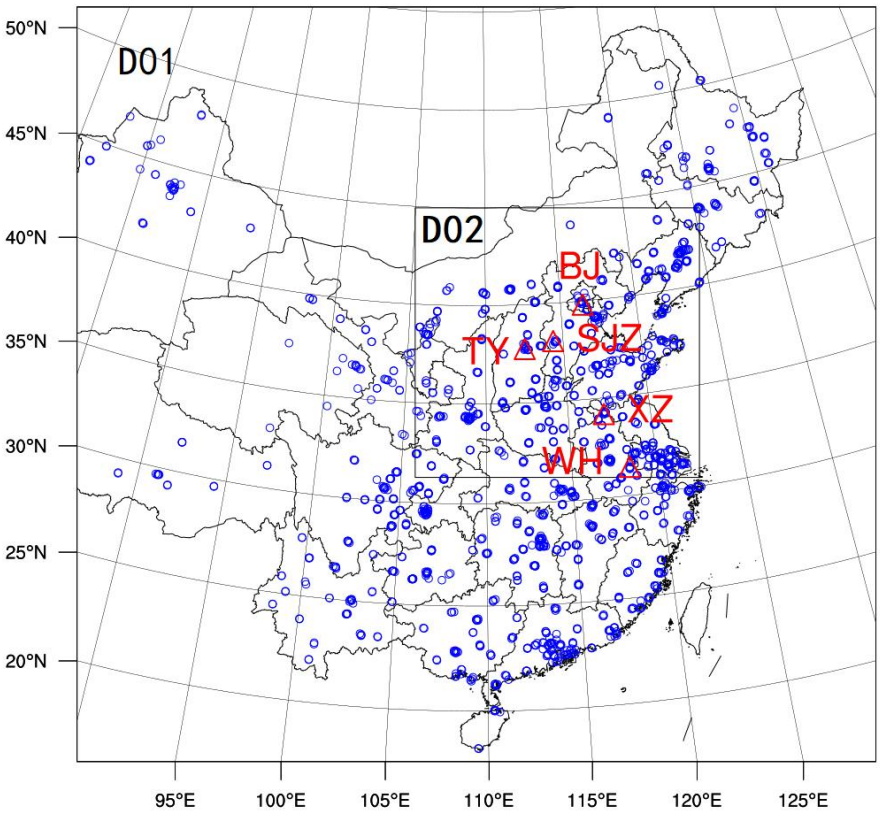

1032

1033 **Figure 1** The double-nested experimental domain. Red triangle and labeling indicate the

1034 locations and names of 5 lidars, and blue circle the locations of 1500 ground environmental

1035 monitoring stations.

1036

1037

1038

1039

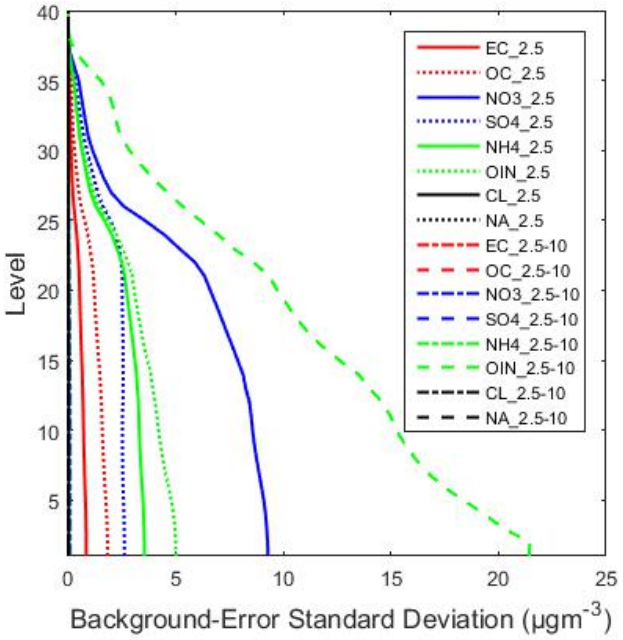

Figure 2 Vertical BESD profiles of the 16 control variables

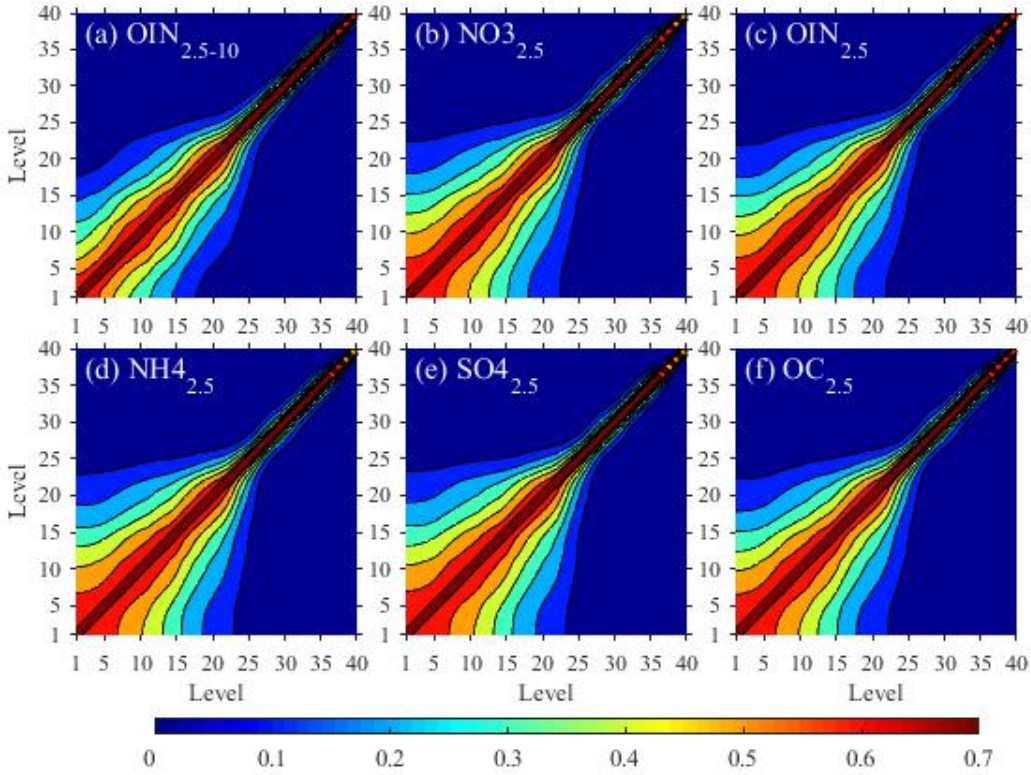

1052

1053 Figure 3 BEVCCs of six control variables

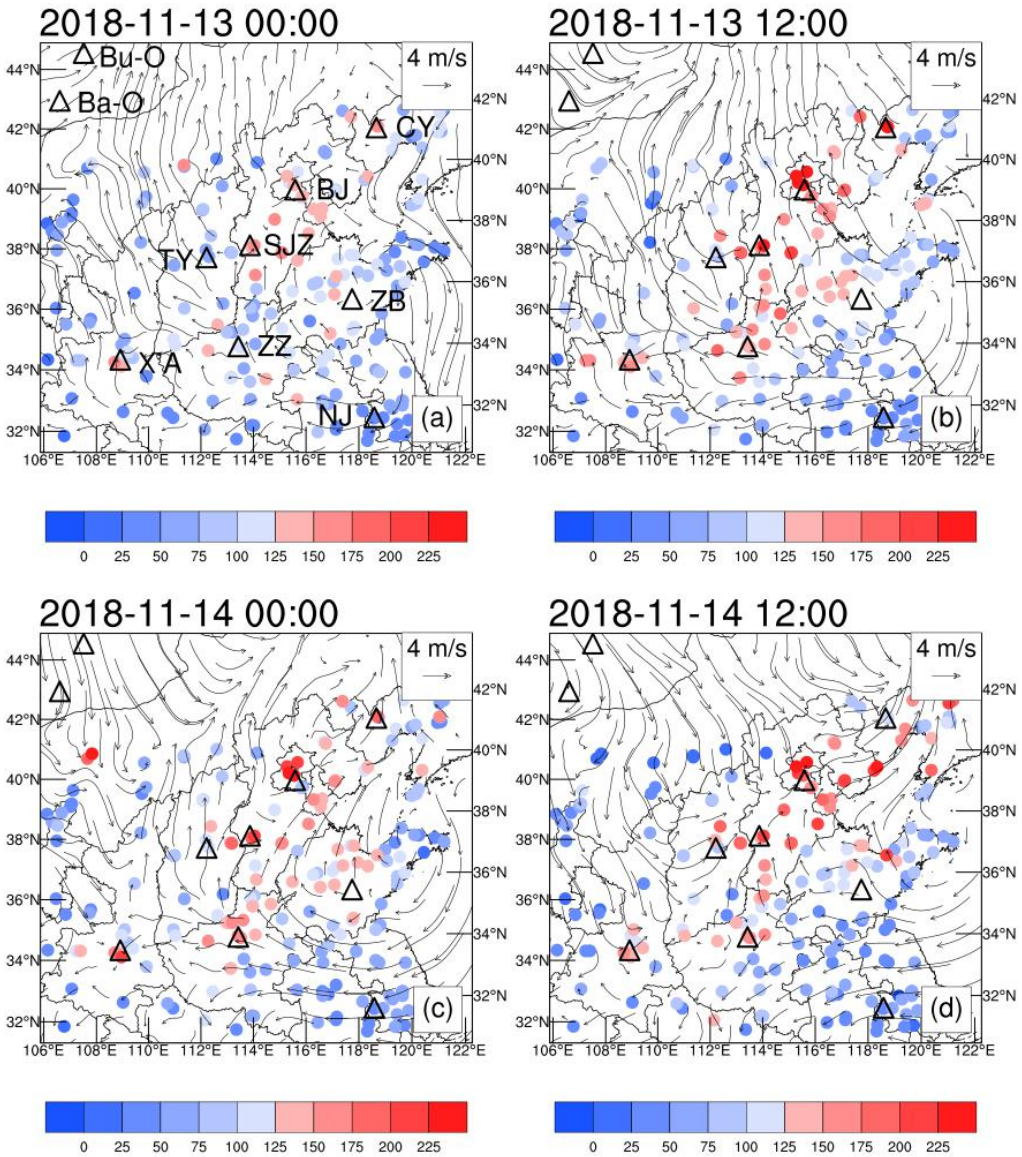

Figure 4 Surface $PM_{2.5}$MC measurements in the D02 region and NCEP reanalysis wind field for the period from 0000 UTC, November 13, 2018 to 1200 UTC, November 14, 2018 (Bu-O: Buyant-Ovoo; Ba-O: Bayan-Ovoo; CY: Chaoyang; BJ: Beijing; SJZ: Shijiazhuang; TY: Taiyuan; ZB: Zibo; X'A: Xi'an; ZZ: Zhengzhou; NJ: Nanjing)

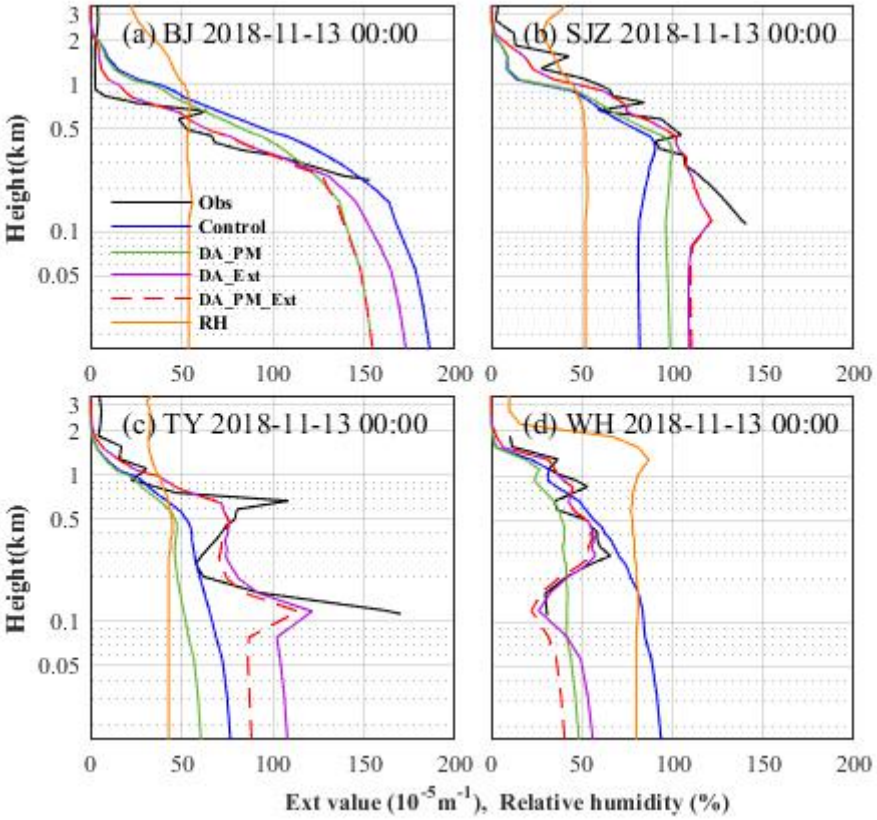

Figure 5 AEC profiles measurements (black lines), the AEC profiles in the analysis fields of the control (blue lines), DA_PM (green lines), DA_Ext (purple lines) and DA_PM_Ext (red lines) experiments and the simulated RH profiles (orange lines) at four lidar stations at 0000 UTC, November 13, 2018. (BJ: Beijing; SJZ: Shijiazhuang; TY: Taiyuan; WH: Wuhu)

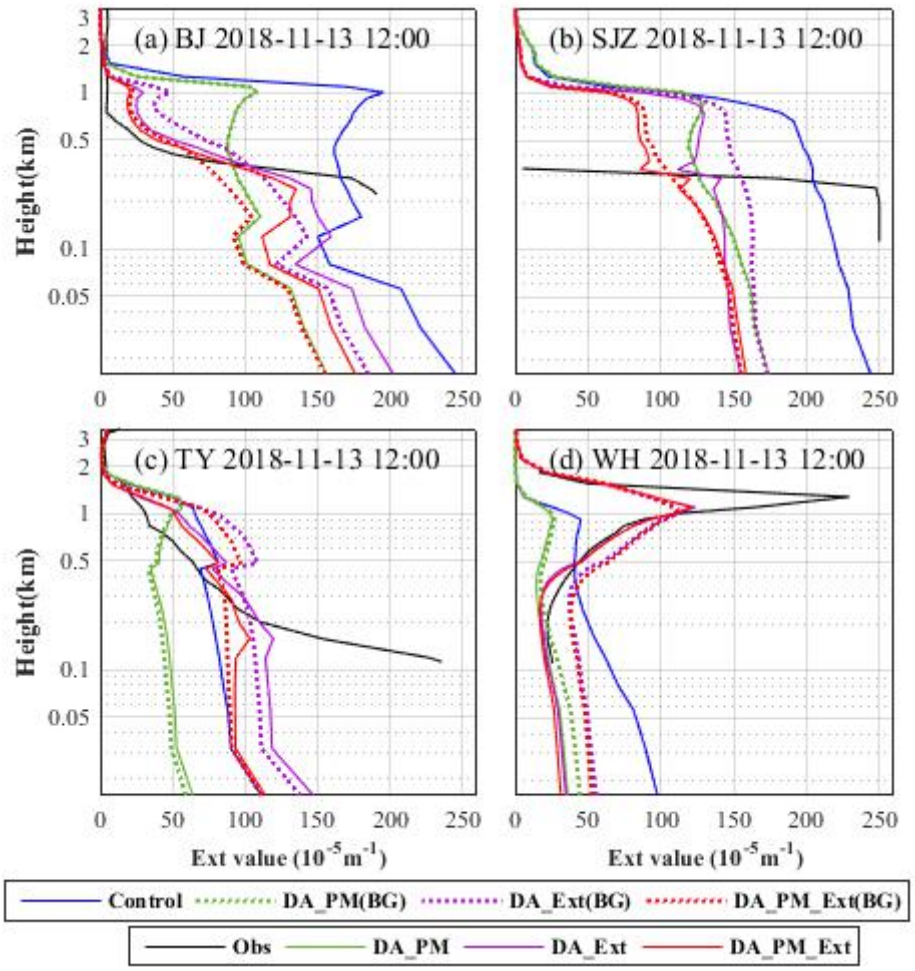

1065

1066 **Figure 6** AEC profiles measurements (solid black lines), the AEC profiles in the control
1067 experiment (solid blue lines), in the background field of the DA_PM (dotted green lines),
1068 DA_Ext (dotted purple lines) and DA_PM_Ext (dotted red lines) experiments, and in the
1069 analysis fields of the DA_PM (solid green lines), DA_Ext (solid purple lines) and
1070 DA_PM_Ext (solid red lines) experiments at four lidar stations at 1200 UTC, November 13,
1071 2018. (BJ: Beijing; SJZ: Shijiazhuang; TY: Taiyuan; WH: Wuhu)

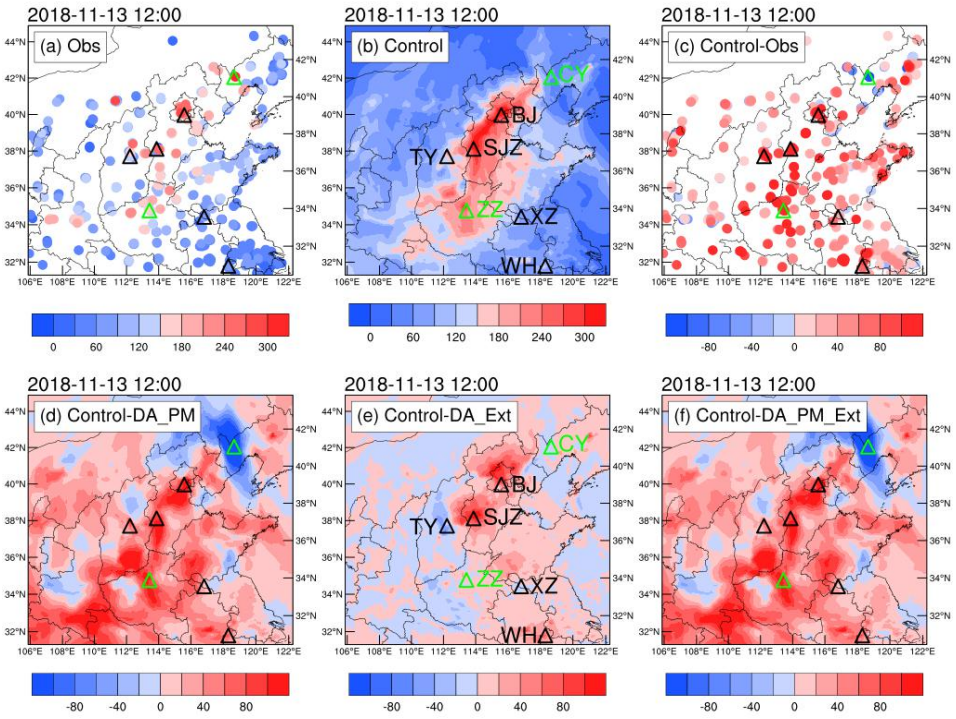

Figure 7 Surface $PM_{2.5}$MC measurements (a), surface $PM_{2.5}$MCs in the initial field of control experiment (b) and its bias (c), the inverse DA increments of $PM_{2.5}$MC of DA experiments, that is, the $PM_{2.5}$MCs obtained from the control experiment minus that from the DA experiments (d, e, and f) at 1200UTC, November 13, 2018 (black triangles signify the locations of the lidar stations, and green triangles mark the locations of the two cities without lidar) (CY: Chaoyang; BJ: Beijing; SJZ: Shijiazhuang; TY: Taiyuan; ZZ: Zhengzhou; XZ: Xuzhou; WH: Wuhu)

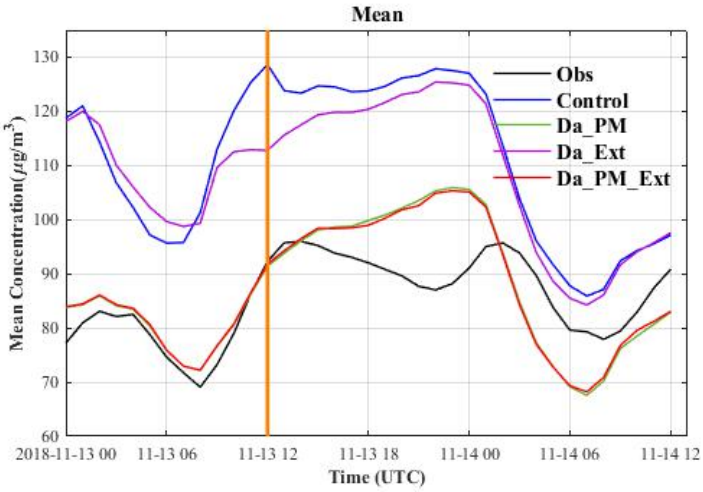

1088

1089 **Figure 8** Variation of the regional mean $PM_{2.5}$MC over time measured and simulated by
1090 the four experiments. (the vertical orange line separates the DA and forecast periods; the
1091 black line signifies measurements; the blue line signifies that obtained from the control
1092 experiment; the green, purple, and red lines signify that obtained from the DA_PM,
1093 DA_Ext, and DA_PM_Ext experiments, respectively)

1094

1095

1096

1097

1098

1099

1100

1101

1102

1103

1104

1105

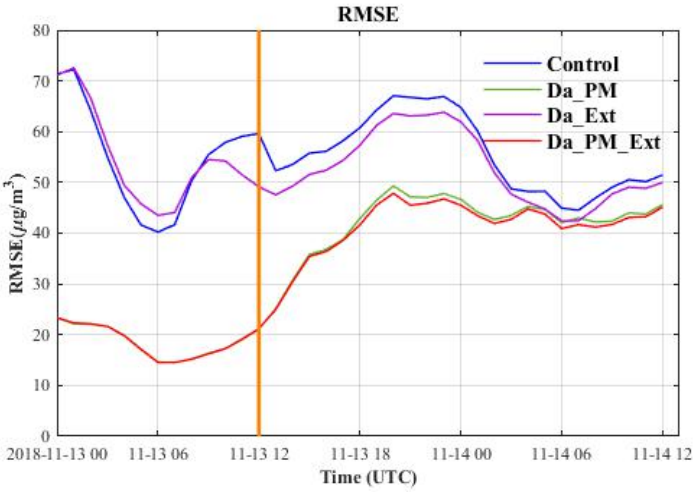

1106

1107 **Figure 9** Variation in the RMSE of surface $PM_{2.5}$MC forecasts over time (the vertical
1108 orange line separates the DA and forecast periods; the blue line signifies that obtained from
1109 the control experiment; the green, purple, and red lines signify that obtained from the
1110 DA_PM, DA_Ext, and DA_PM_Ext experiments, respectively)

1111